

Unsupervised Multi-Parameter Inverse Solving for Reducing Ring Artifacts in 3D X-Ray CBCT

Qing Wu¹ Hongjiang Wei² Jingyi Yu¹ Yuyao Zhang^{1§}

¹ShanghaiTech University ²Shanghai Jiao Tong University

{wuqing, yujingyi, zhangyy8}@shanghaitech.edu.cn, hongjiang.wei@sjtu.edu.cn

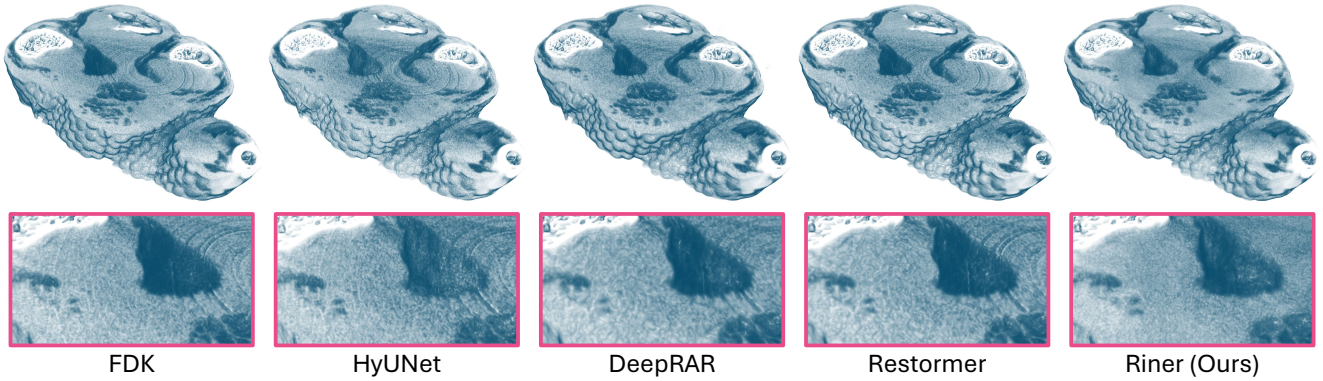


Figure 1. We propose Riner, an unsupervised method for reducing ring artifacts in 3D X-ray CBCT imaging. On a real-world *Chicken foot* sample (Fig. 4 Right) with image dimension of $512 \times 512 \times 80$ and an ultra-high resolution of $60 \times 60 \times 60 \mu\text{m}^3$, acquired by a commercial Bruker SKYSCAN 1276 micro-CT scanner, our Riner effectively removes ring artifacts and reconstructs high-quality CT volumes, outperforming traditional linear algorithm (FDK [14]) and SOTA supervised (HyUNet [6], DeepRAR [50], and Restormer [60]) techniques.

Abstract

Ring artifacts are prevalent in 3D cone-beam computed tomography (CBCT) due to non-ideal responses of X-ray detectors, severely degrading imaging quality and reliability. Current state-of-the-art (SOTA) ring artifact reduction (RAR) algorithms rely on extensive paired CT samples for supervised learning. While effective, these methods do not fully capture the physical characteristics of ring artifacts, leading to pronounced performance drops when applied to out-of-domain data. Moreover, their applications to 3D CBCT are limited by high memory demands. In this work, we introduce **Riner**, an unsupervised method formulating 3D CBCT RAR as a multi-parameter inverse problem. Our core innovation is parameterizing the X-ray detector responses as solvable variables within a differential physical model. By jointly optimizing a neural field to represent artifact-free CT images and estimating response parameters directly from raw measurements, Riner eliminates the need for external training data. Moreover, it accommodates diverse CT geometries, enhancing practical usability. Empirical results on both simulated and real-world datasets

show that Riner surpasses existing SOTA RAR methods in performance.

1. Introduction

3D cone-beam computed tomography (CBCT) enables detailed visualization of internal structures, providing critical information for applications ranging from medical diagnosis and biological research to materials science [43, 51]. CBCT acquisition involves a series of 2D projections captured by a 2D X-ray detector array at varying angles, as illustrated in Fig. 2. However, due to inherent physical hardware limitations [4, 34], individual detectors within the 2D array often struggle to maintain ideal, consistent signal responses, especially in μm -scale imaging using micro-CT scanners [22, 36, 37, 59]. These non-ideal responses lead to nonlinear physical distortions in the measurement data, producing severe ring artifacts when traditional linear reconstruction algorithms (e.g., FDK [14]) are applied. Such artifacts can markedly degrade the quality and reliability of the resulting CT images.

Current supervised deep learning (DL) methods [6, 13,

26, 31, 50, 60] represent the state-of-the-art (SOTA) for ring artifact reduction (RAR). These approaches train deep neural networks, such as UNet [41] and ViT [11], on extensive paired datasets to map artifact-laden images to artifact-free outputs. Although effective, these methods share two significant limitations. **1) High data collection costs and limited generalization.** Collecting paired CT images is often prohibitively expensive, especially for medical and biological applications. Hence, models are generally trained on simulated datasets derived from artifact-free CT images [13, 26]. However, simulation errors (*e.g.*, differences in image resolution, detector characteristics, and CT geometry) can substantially degrade performance on real-world data. **2) Memory constraints in 3D CBCT.** Most SOTA methods [31, 50] encounter difficulties when applied to 3D CBCT due to high memory requirements. Approaches that adapt 2D models by processing slice-by-slice often result in discontinuities along the Z-axis, undermining 3D image consistency. These constraints restrict the use of supervised DL models primarily to controlled research settings, limiting their practical utility in broader applications.

In this paper, we introduce **Riner**, a novel unsupervised approach for 3D CBCT RAR. Riner treats RAR as a multi-parameter inverse problem, parameterizing the signal responses of X-ray detectors as variables to be optimized. By accurately estimating these response parameters, Riner fundamentally eliminates the nonlinear effects that cause ring artifacts, enabling robust artifact-free reconstructions. Riner leverages a novel differential physical model to characterize the non-ideal behavior of X-ray detectors, jointly optimizing neural fields [28] to represent high-quality CT images while estimating response parameters directly from raw measurements, without relying on external training data. The inherent spectral bias of neural fields, *i.e.*, favoring low-frequency image patterns [28, 35, 56], effectively mitigates the challenges of this ill-posed inverse problem, resulting in accurate solutions. Moreover, Riner is adaptable to various scanner types (*e.g.*, 2D fan-beam (FB), 3D CBCT, and helical CT) through simple modifications to incorporate specific CT geometries, enhancing its versatility across different imaging setups.

We evaluate the RAR performance of Riner on five datasets, comprising three simulated datasets and two real-world datasets, under both 2D fan-beam (FBCT) and 3D CBCT protocols. Experimental results show that our unsupervised method consistently surpasses existing SOTA model-based and supervised RAR techniques across all cases. Extensive ablation studies validate the effectiveness of each key component of our model. *To our knowledge, Riner is the first unsupervised RAR method to achieve performance that exceeds that of supervised approaches.*

The main contributions of this paper are as follows:

- We provide a theoretical analysis of the physical origins

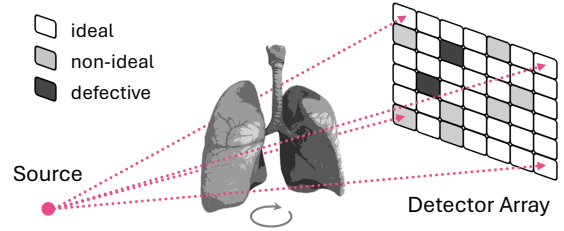


Figure 2. Illustration of 3D CBCT acquisition. An X-ray source emits cone-shaped beams, which pass through objects and are then received by a 2D X-ray detector array. Due to physical hardware limitations [4, 34], there are three types of detectors: ideal detectors (white), non-ideal detectors with fluctuating responses (gray), and defective detectors without responses (black).

of CT ring artifacts and propose a new multi-parameter solving framework to address the RAR problem.

- We propose **Riner**, a novel unsupervised RAR method that jointly recovers high-quality CT images and estimates detector responses from CT measurements.
- We perform extensive experiments on both simulated and real-world data, confirming the superiority of our unsupervised Riner over SOTA RAR techniques.

2. Related Work

In this section, we briefly review advances for CT ring artifact reduction (Sec. 2.1), multi-parameter inverse problem (Sec. 2.2), and neural fields for CT imaging (Sec. 2.3).

2.1. Advances for Ring Artifact Reduction

Many attempts have been made for ring artifact reduction (RAR) [8]. Early model-based approaches [30, 37, 40, 49, 52] use well-designed filters to correct CT measurements, but achieve limited RAR performance due to handcrafted priors. Recently, supervised DL methods [6, 13, 26, 31, 50, 60] have shown significant improvements over model-based methods by leveraging data-driven priors. However, both model-based and supervised methods address RAR as a post-processing task, lacking effective modeling for the physical nature of ring artifacts, which limits their generalization. In contrast, we treat RAR as a multi-parameter inverse problem within a physics-driven framework, leading to improved robustness and generalization.

2.2. Multi-Parameter Inverse Problem

Multi-parameter inverse problems (MPIPs) involve estimating multiple unknown parameters of a complex system from measurement data. By incorporating domain-specific physical prior knowledge, MPIPs-based approaches have shown promising potential in various fields, including physics [9, 10, 64], partial differential equations [7, 16], remote sensing [21, 58], and more. Inspired by the suc-

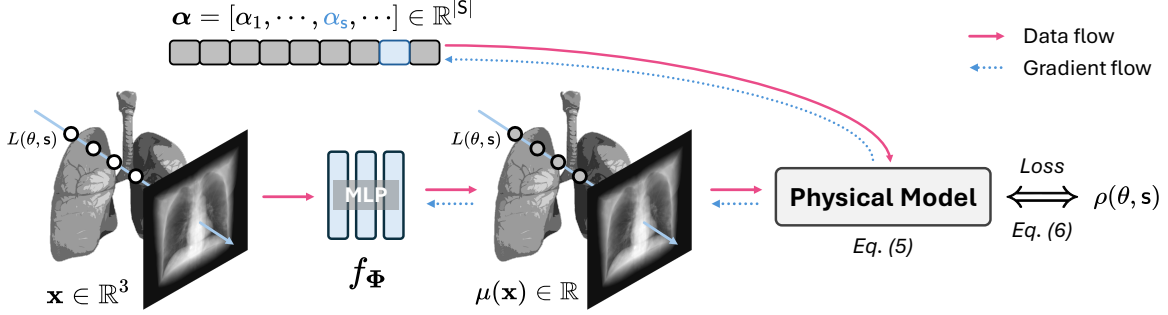


Figure 3. Overview of the proposed Riner method. Given CT measurements $\rho(\theta, s)$, an MLP network f_{Φ} receives multiple spatial coordinates \mathbf{x} along an X-ray path $L(\theta, s)$ as input and predicts the corresponding CT intensities $\mu(\mathbf{x}) = f_{\Phi}(\mathbf{x})$. These predicted intensities, $\mu(\mathbf{x}), \forall \mathbf{x} \in L(\theta, s)$ and the response parameter α_s are then used to generate estimated measurements $\hat{\rho}(\theta, s)$ via a differential physical model (Eq. 5). Finally, the MLP network f_{Φ} and parameter α_s jointly are optimized by minimizing errors (Eq. 6) between the estimated and real measurements.

cess of MIPs-based solutions, we theoretically analyze the physical mechanisms of ring artifacts and develop an unsupervised MIPs-based RAR framework that significantly improves CT reconstructions.

2.3. Neural Fields for CT Imaging

Neural radiance field (NeRF) [28] is a revolutionary technique in novel view synthesis. Using a differential volume rendering model, NeRF optimizes an MLP to learn a continuous function that represents a scene from limited view images. Recently, unsupervised NeRF-based methods have shown promise in various CT applications, such as undersampling CT [5, 12, 42, 44, 54, 61, 62], dynamic CT [3, 38, 63], and metal artifact reduction [24, 53, 55]. However, these methods cannot address the RAR problem, as they generally consider CT acquisition process as a linear integral model, thereby overlooking the nonlinear effects of non-ideal detectors. Instead, our Riner introduces a new physical model that characterizes non-ideal detectors by explicitly estimating response parameters, enabling effective RAR reconstruction.

3. Methodology

In this section, we first analyze the physical nature of ring artifacts, providing key insights for our method (Sec. 3.1). Then, we present our problem formulation (Sec. 3.2) and a new physical model (Sec. 3.3). Finally, we introduce model optimization (Sec. 3.4), as shown in Fig. 3.

3.1. Theoretical Analysis for Ring Artifacts

The Lambert-Beer’s law [2, 23] formulates the basic physical process of X-ray CT acquisition as below:

$$I(\theta, s) = \alpha_s \cdot I_0 \cdot \exp\left(-\int_{L(\theta, s)} \mu(\mathbf{x}) d\mathbf{x}\right), \quad (1)$$

where $L(\theta, s)$ denotes an X-ray received by an X-ray detector s at a projection view θ , and $I(\theta, s)$ is the number of received photons. I_0 is the number of photons emitted by an X-ray source. $\alpha_s \geq 0$ is the response factor of the detector s , measuring its detection ability. $\mu(\mathbf{x})$ represents the attenuation coefficient of objects at the position \mathbf{x} .

By assuming ideal X-ray detectors (*i.e.*, $\alpha_s = 1, \forall s$), CT measurement data can be defined as:

$$\rho(\theta, s) \triangleq -\ln \frac{I(\theta, s)}{\alpha_s \cdot I_0} = \int_{L(\theta, s)} \mu(\mathbf{x}) d\mathbf{x}. \quad (2)$$

Then, one can reconstruct high-quality CT images μ from the measurement data ρ using linear reconstruction algorithms, such as FDK [14].

However, in practice, the responses of X-ray detectors are often non-ideal and difficult to maintain consistently (*i.e.*, $\alpha_s \neq 1, \forall s$, and $\alpha(s_a) \neq \alpha(s_b), \forall s_a, s_b \in S$, where S is the set of the detectors) due to hardware limitations [4, 34]. The measurement data is thus given by

$$\rho(\theta, s) = \begin{cases} -\ln \alpha_s + \int_{L(\theta, s)} \mu(\mathbf{x}) d\mathbf{x}, & \text{if } \alpha_s > 0 \\ \text{NaN}, & \text{if } \alpha_s = 0 \end{cases}, \forall s. \quad (3)$$

From Eq. (3), we observe two physical effects:

- **Inconsistent responses (IR)**, where non-ideal detectors (*i.e.*, $\alpha_s > 0$ and $\alpha_s \neq 1$) introduce nonlinear transformations $-\ln \alpha_s$ in the measurement data;
- **Invalid measurements (IM)**, where partial measurement data acquired by defective detectors (*i.e.*, $\alpha_s = 0$) are invalid.

These two physical effects make the inverse problem of reconstructing the unknown CT images μ from the measurements ρ inherently nonlinear. Therefore, traditional linear algorithms, such as FDK [14], are prone to severe ring artifacts in CT reconstructions.

3.2. Problem Formulation

Existing RAR algorithms [6, 30, 50, 52, 60] mostly address an image denoising task from a post-processing perspective, lacking efficient modeling for the physical nature of ring artifacts and producing limited generalization.

In contrast, this work treats RAR as a multi-parameter inverse problem. We argue that a physics-driven framework can achieve improved performance and generalization. As highlighted in our theoretical analysis (Sec. 3.1), the IR and IM effects are fundamental causes of ring artifacts. To address these, we propose parameterizing the response factors of X-ray detectors (including ideal, non-ideal, and defective types) as a vector $\alpha = [\alpha_1, \dots, \alpha_s, \dots] \in \mathbb{R}^{|\mathcal{S}|}$, which will be solved. By accurately estimating the response vector α , both IR and IM effects can be effectively mitigated. Our objective, therefore, is to jointly reconstruct the unknown CT image μ and estimate the response vector α from the measurement data ρ in an *unsupervised* manner.

Due to the introduction of additional response parameters, this inverse problem (*i.e.*, $\rho \Rightarrow \{\alpha, \mu\}$) is highly ill-posed, where multiple feasible solutions exist. In our model, we leverage the neural field [28] to parametrize the CT image μ . Specifically, we represent the CT image as a continuous function parametrized by an MLP network as:

$$\mu(\mathbf{x}) = f_{\Phi}(\mathbf{x}), \quad (4)$$

where Φ denote the learnable weights of the MLP network. Many studies [28, 35, 46, 48] have demonstrated that neural networks, when used to approximate a natural image, typically capture low-frequency global structures first and then gradually recover high-frequency details. We aim to leverage this inherent learning prior to constrain the solution space of the ill-posed inverse problem, resulting in excellent CT reconstructions.

3.3. Physical Model for IR and IM Effects

In line with the above formulation, we optimize the MLP network f_{Φ} to learn the function that maps spatial coordinates \mathbf{x} to CT intensities $\mu(\mathbf{x})$. To achieve this, we introduce a new *differential* physical model, which converts these MLP-predicted intensities $\mu(\mathbf{x})$ and the response factor α_s into CT measurement data $\rho(\theta, s)$, while allowing for gradient back-propagation. Building on the theoretical results in Eq. 3, the physical model is defined as follows:

$$\rho(\theta, s) = \left[-\ln(\max(\alpha_s, 0) + \epsilon) + \sum_{\mathbf{x} \in L(\theta, s)} \mu(\mathbf{x}) \cdot \Delta \mathbf{x} \right] \cdot \mathbf{m}(s), \quad (5)$$

where $\epsilon = 10^{-8}$ is a constant ensuring valid logarithmic calculations, and $\Delta \mathbf{x} = \|\mathbf{x}_a - \mathbf{x}_b\|_2$ represents the Euclidean distance between adjacent coordinates $\mathbf{x}_a, \mathbf{x}_b \in$

$L(\theta, s)$ along the X-ray path. $\mathbf{m} \in \mathbb{R}^{|\mathcal{S}|}$ is a binary mask vector, where $\mathbf{m}(s) = 0$ for defective detectors (*i.e.*, $\alpha_s = 0$) and 1 otherwise. The mask \mathbf{m} is generated by simply applying edge filters to the projection data.

Superior to conventional linear integral models [25, 44, 54, 61, 62], our physical model effectively addresses the CT RAR problem by introducing additional physical parameters for more accurate acquisition modeling. Specifically, it includes **1) Parameterization of the detector responses**, where our model explicitly estimates the response vector α to alleviate the IR effect; **2) Removing of invalid measurements**, where we employ the mask \mathbf{m} to block the gradient back-propagation from invalid signals measured by defective X-ray detectors, thereby eliminating the IM effect.

3.4. Model Optimization

Fig. 3 shows the optimization pipeline to our Riner model. We first sample a set of spatial coordinates \mathbf{x} along the X-ray $L(\theta, s)$ at a pre-defined and fixed interval $\Delta \mathbf{x}$. Then, we feed them into the MLP network f_{Φ} to predict the corresponding CT intensities $\mu(\mathbf{x})$. Furthermore, we conduct our differential physical model (Eq. 5) to convert these MLP-predicted intensities $\mu(\mathbf{x}) = f_{\Phi}(\mathbf{x}), \forall \mathbf{x} \in L(\theta, s)$ and corresponding learnable response factor α_s into estimated projection $\hat{\rho}(\theta, s)$. Finally, the MLP network f_{Φ} and response parameter α_s simultaneously are optimized by minimizing the loss function, which is defined as:

$$\mathcal{L} = \sum_{\theta \in \Theta} \sum_{s \in \mathcal{S}_{\text{sub}}} \|\rho(\theta, s) - \hat{\rho}(\theta, s)\|_1 \quad (6)$$

where Θ and $\mathcal{S}_{\text{sub}} \subseteq \mathcal{S}$ are random subsets of projection angles and detectors, respectively, at each step.

After model optimization, the MLP network f_{Φ} and the vector α represent the desired CT image and detector responses, respectively. We recover the high-quality CT image μ by feeding all coordinates \mathbf{x} into the network.

Implementation Details We implement our model using PyTorch [33]. The network f_{Φ} includes hash encoding [29] and two fully connected (FC) layers, with a ReLU function following the first FC layer. The hash encoding can accelerate optimization and improve high-frequency detail reconstruction. We use the hyperparameters referenced from the original paper [29]: $L = 16$, $T = 2^{18}$, $F = 8$, $N_{\text{min}} = 2$, and $b = 2$. At each iteration, 80 X-rays from 2 detectors across 40 projection views are randomly sampled, *i.e.*, $|\mathcal{S}_{\text{sub}}| = 2$ and $|\Theta| = 40$. The Adam optimizer [20] with default settings is used. The learning rate is 10^{-3} , decaying by 0.5 every 1,000 iterations, over a total of 4,000 iterations. All hyperparameters are tuned on 10 samples from DeepLesion dataset [57] and remain fixed for all others.

Table 1. Quantitative results of our Riner and baselines on three simulated datasets (2D FBCT DeepLesion [57] and 2D FBCT LIDC [1], and 3D CBCT AAPM [27]). The top-two performances are highlighted in **bold** and underline, respectively.

Category	Method	DeepLesion [57]		LIDC [1]		AAPM [27]	
		PSNR	SSIM	PSNR	SSIM	PSNR	SSIM
Linear	FBP/FDK [14, 18]	13.81±3.01	0.505±0.129	12.29±2.86	0.452±0.153	17.96±1.04	0.799±0.040
	Norm [40]	24.37±1.95	0.774±0.067	24.61±2.31	0.786±0.049	29.05±0.28	0.906±0.012
Model-based	WaveFFT [30]	20.70±2.48	0.663±0.096	19.44±2.22	0.622±0.118	26.65±0.97	0.858±0.031
	Super [52]	29.11±3.43	0.815±0.084	31.24±3.14	0.855±0.051	32.83±4.17	0.937±0.024
Supervised	HyUNet [6]	33.73±1.88	0.893±0.035	32.46±1.54	0.854±0.051	33.76±0.96	0.923±0.019
	DeepRAR [50]	34.61±2.13	0.893±0.043	30.34±3.54	0.802±0.085	29.53±0.90	0.871±0.030
	Restormer [60]	37.31±1.92	0.947±0.028	36.69±1.90	0.925±0.051	36.52±0.57	0.957±0.010
Unsupervised	SinoRAR [45]	32.70±1.77	0.881±0.034	32.63±1.21	0.879±0.035	N/A	N/A
	Riner (Ours)	38.93±2.21	0.965±0.021	38.83±2.14	0.958±0.033	37.27±1.30	0.977±0.008

4. Experiments

In this section, we conduct extensive experiments to assess our unsupervised method, including 1) comparisons (Sec. 4.2 & Sec. 4.3) with SOTA RAR approaches on both simulated and real-world data, and 2) ablation studies on the key components of our model (Sec. 4.4). Further experimental details and results are available in the Appendix.

4.1. Experimental Settings

Dataset We perform our experiments on three simulated datasets and two real-world datasets, as follows:

- **Simulated 2D FBCT DeepLesion [57]**, consisting of 5,261 2D slices of a 256×256 size from multiple 3D volumes. We split these 2D slices into three parts: 5,061 slices for training set, 100 slices for validation set, and 100 slices for test set. *Notably, our unsupervised Riner does not access the training and validation sets used for training supervised baselines.*
- **Simulated 2D FBCT LIDC [1]**, consisting of 100 2D slices of a 256×256 size from multiple 3D volumes for an additional test set.
- **Simulated 3D CBCT AAPM [27]**, consisting of 10 3D volumes, each with sizes of $256 \times 256 \times 100$, used to evaluate our Riner model and baselines within 3D CBCT geometry.
- **Real-world 2D FBCT Walnut**, consisting of a 2D slice with sizes of 512×512 and a physical resolution of $60 \times 60 \mu\text{m}^2$, acquired by a commercial Bruker SKYSCAN 1276 micro-CT scanner using 2D FBCT geometry.
- **Real-world 3D CBCT Chicken foot**, consisting of a 3D volume with sizes of $512 \times 512 \times 80$ and a physical resolution of $60 \times 60 \times 60 \mu\text{m}^3$, acquired by a commercial Bruker SKYSCAN 1276 micro-CT scanner using 3D CBCT geometry.

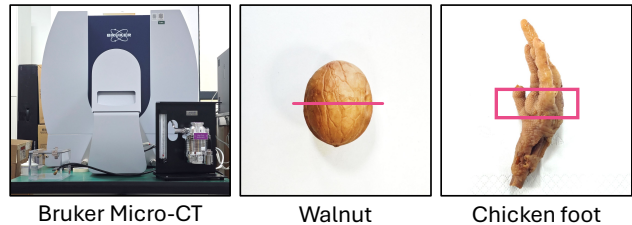


Figure 4. (Left) A commercial Bruker SKYSCAN 1276 micro-CT scanner used for measuring real-world CT projection data. (Middle & Right) Walnut and Chicken foot samples used in our 2D FBCT and 3D CBCT real-world experiments. Here the pink line and box denote the ROIs to be reconstructed.

Data Pre-processing For the three simulated datasets, we follow the workflows in [6, 45, 50] to simulate ring artifacts. Specifically, 75% of the X-ray detectors randomly are considered non-ideal, with their response factors α_s ranging from [0.75, 1.25], and two detectors are set as defective (*i.e.*, $\alpha_s = 0$). We use the Python library CIL [17, 32] to simulate 2D FBCT and 3D CBCT acquisition geometries. Moreover, noise are simulated in the projection data. For the two real-world datasets, we use a commercial Bruker SKYSCAN 1276 micro-CT scanner under 2D FBCT and 3D CBCT protocols, as shown in Fig. 4. Additional details about data pre-processing are provided in the Appendix.

Baselines and Metrics We compare our method against nine SOTA RAR methods, including 1) traditional linear reconstruction algorithms (FBP [18] and FDK [14]); 2) model-based algorithms (Norm [40], WaveFFT [30], and Super [52]); 3) supervised DL models (HyUNet [6], DeepRAR [50], and Restormer [60]); 4) an unsupervised DL model (SinoRAR [45]). The three supervised methods (HyUNet [6], DeepRAR [50], and Restormer [60]) are trained using the training and validation sets of the DeepLe-

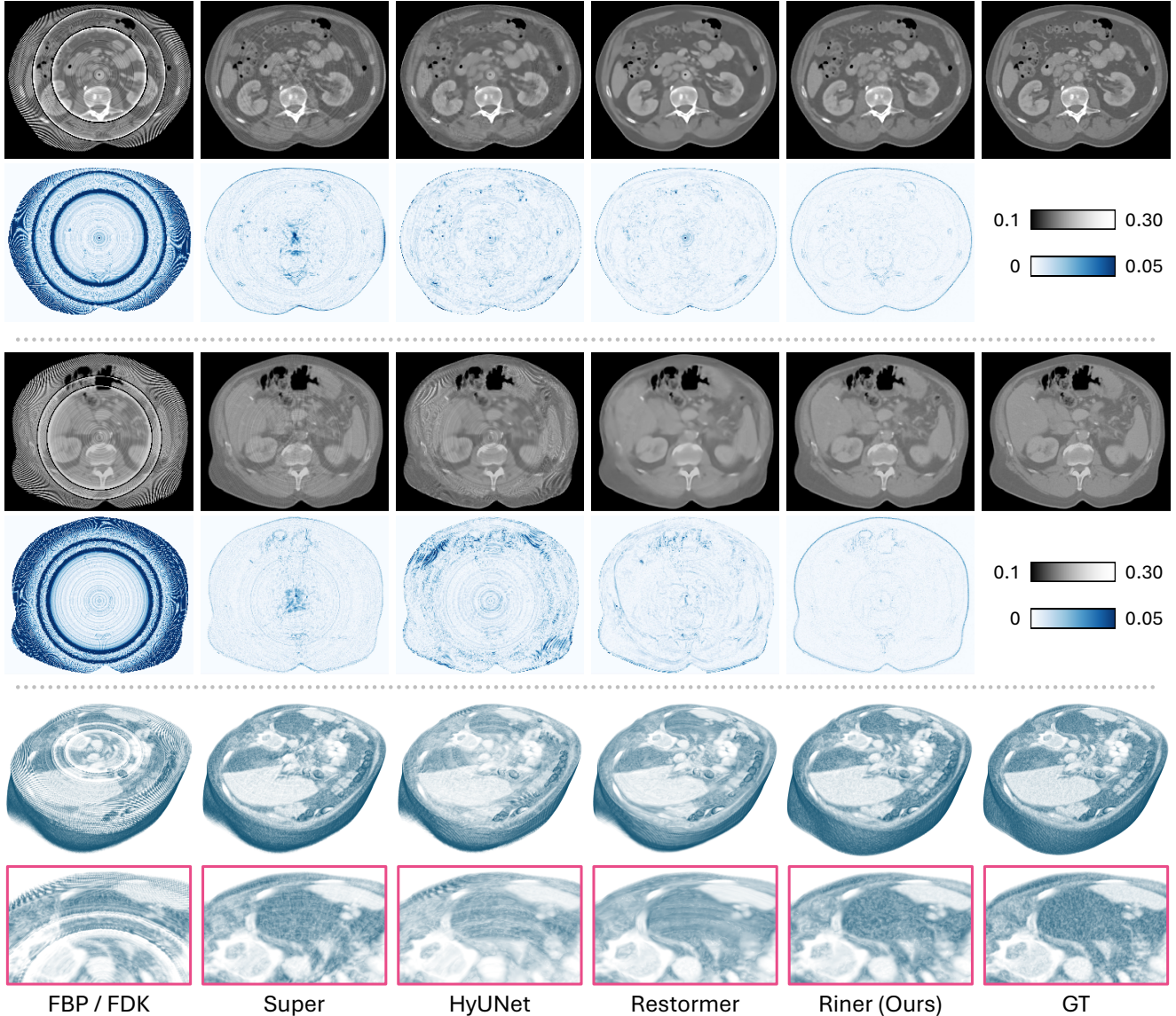


Figure 5. Qualitative results of our Riner and baselines on three representative samples of three simulated datasets (2D FBCT DeepLesion [57] and 2D FBCT LIDC [1], and 3D CBCT AAPM [27]).

sion dataset [57]. Moreover, we use PSNR and SSIM as quantitative metrics to measure model performance.

4.2. Comparisons on Simulated Datasets

We first compare our Riner with nine baselines on three simulated datasets. Note that the three supervised baselines (HyUNet [6], DeepRAR [50], and Restormer [60]) are specifically designed for 2D CT. In our experiments, we apply these 2D models slice-by-slice to reconstruct 3D volumes. Since SinoRAR [45] operates on 2D measurement data, we exclude it from comparisons on 3D datasets.

Quantitative Results Tab. 1 shows the quantitative comparisons. Overall, our Riner consistently obtains the best performance across the three simulated datasets, outperforming the SOTA supervised Restormer [60] based on ViT [11], with PSNR improvements of +1.62 dB, +2.14 dB, and +0.75 dB, respectively. Among the four model-based algorithms, Super [52] achieves the highest quantitative results but still falls slightly behind the unsupervised SinoRAR method [45]. While the supervised HyUNet [6] and DeepRAR (based on convolutional UNet [41]) perform well on the DeepLesion dataset [57], they encounter the OOD problem, resulting in significant performance drops when tackled with the unseen LIDC [1] and AAPM [27] datasets.

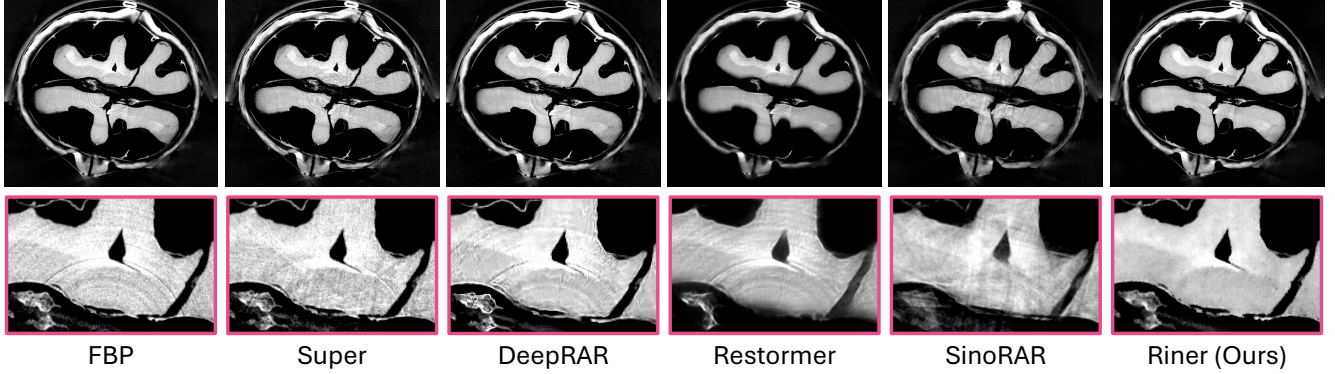


Figure 6. Qualitative results of our Riner and baselines on a real-world *Walnut* sample (Fig. 4 *Middle*) with sizes of 512×512 and an ultra-high resolution of $60 \times 60 \mu\text{m}^2$, acquired by a commercial Bruker SKYSCAN 1276 micro-CT scanner.

Table 2. Quantitative errors (Mean \pm STD) of ideal, our predicted, and GT responses on three simulated datasets.

Dataset	Ideal Responses	Our Estimations
DeepLesion [57]	0.093 \pm 0.083	0.012\pm0.022
LIDC [1]	0.093 \pm 0.083	0.011\pm0.021
AAPM [27]	0.094 \pm 0.083	0.017\pm0.021

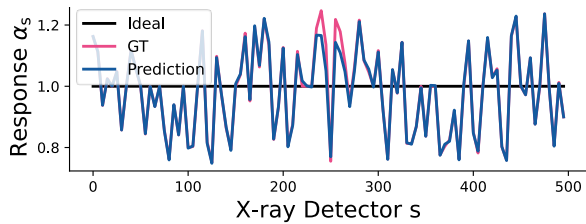


Figure 7. Visualization of ideal, our predicted, and GT responses α on a test sample (#9) of DeepLesion dataset [57].

In contrast, our Riner achieves superior and stable RAR reconstructions across different datasets, benefiting from its physics-driven solving framework.

The effectiveness of our method in addressing the RAR problem mainly lies in its explicit estimation of detector responses. In Fig. 7, we visualize the ideal, predicted, and ground truth (GT) detector responses on a representative test sample from the 2D FBCT DeepLesion dataset [57]. The response parameters estimated by our Riner are significantly close to the GT values. Tab. 2 also quantitatively shows that accurate responses are stably estimated across the three simulated datasets.

Qualitative Results We present the qualitative comparisons in Fig. 5. The reconstructions produced by linear algorithms (FBP [18] and FDK [14]) exhibit severe ring artifacts due to neglecting non-ideal detector responses. The model-based Super [52] reduces major ring artifacts but introduces

additional artifacts. On the DeepLesion dataset [57], the supervised methods HyUNet [6] and Restormer achieve notable improvements over Super [52] in terms of artifact removal and image detail preservation. However, on the unseen LIDC [1] and AAPM [27] datasets, their reconstructions display severe artifacts and lose many tissue details. These visual results align with the quantitative findings. In contrast, our Riner consistently recovers clear, fine-detail CT images across all three datasets, demonstrating its superiority and robustness over SOTA supervised approaches.

4.3. Comparisons on Real-World Datasets

Micro-CT imaging is widely used in fields such as biomedical research and materials science [39]. However, ring artifacts are common in Micro-CT due to its μm -level ultra-high physical resolution [22, 36, 37, 59]. Here, we validate the effectiveness of our Riner on the real-world Micro-CT imaging. We scan a *Walnut* sample and a *Chicken foot* sample using a commercial Bruker SKYSCAN 1276 micro-CT scanner under 2D FBCT and 3D CBCT. Detailed acquisition protocols can be found in the Appendix.

We only report qualitative results since GT images are difficult to obtain. As shown in Fig. 1 and Fig. 6, our Riner effectively removes ring artifacts while preserving image details, significantly outperforming baselines. The hyper-parameters for our method remain consistent across simulated and real-world data, demonstrating its robustness.

4.4. Ablation Studies

Physical Model The proposed physical model employ the defective mask \mathbf{m} and the response vector α to tackle the IM and IR effects, respectively. Here we investigate their effectiveness. Fig. 8 shows the qualitative results.

- **Integral model** (*i.e.*, without the vector α and the mask \mathbf{m} , our physical model is degraded as traditional linear integral model). We observe that although the integral model reduces some ring artifacts using the continuous

Table 3. Quantitative results of our Riner ablating the physical model (Eq. 5) on 10 samples of DeepLesion dataset [57].

Physical Model		PSNR	SSIM
Def. mask m	Res. vector α		
✗	✗	35.84±2.20	0.926±0.028
✗	✓	32.65±5.79	0.923±0.049
✓	✗	36.02±1.84	0.933±0.021
✓	✓	38.90±1.37	0.972±0.006

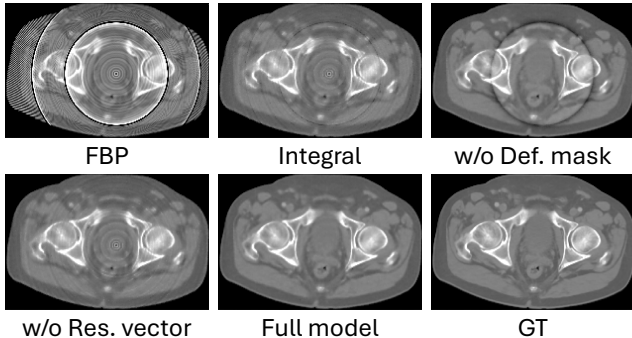


Figure 8. Qualitative results of our Riner ablating the physical model (Eq. 5) on a test sample (#6) of DeepLesion dataset [57].

prior of the MLP network, it still contains significant artifacts due to the IM and IR effects.

- **w/o Defective mask m .** When removing the defective mask, our Riner fail to handle the IM effect. The reconstructed CT image contains black ring artifacts caused by the IM effect, while the minor artifacts of the IR effect effectively are reduced by using the response vector.
- **w/o Res. vector α .** This case is opposite to the scenario 2, where the IM effect artifacts are removed, but artifacts from the IR effect remain.
- **Full model.** Our Riner can effectively eliminate both types of ring artifacts.

We show the quantitative results in Tab. 3. The results further confirm these observations. Generally, the results of ablating the physical model perfectly align with expectations of our physical modeling for the IR and IM effects, demonstrating its effectiveness.

Network Architecture Our network f_{Φ} consists of the hash encoding [29] and an 2-layer MLP. Here, we discuss the influence of network architecture on RAR reconstructions. To this end, we implement the network with Fourier encoding [48] followed by a 4-layer MLP, while keeping other model settings identical for a fair comparison. Tab. 4 presents the quantitative results, where the hash encoding [29] achieves better performance on both metrics. We also provide a qualitative comparison in Fig. 9, showing

Table 4. Quantitative results of our Riner ablating the MLP network on 10 samples of DeepLesion dataset [57].

Network	PSNR	SSIM
Fourier encoding [48]	37.85±2.02	0.968±0.009
Hash encoding [29]	38.90±1.37	0.972±0.006

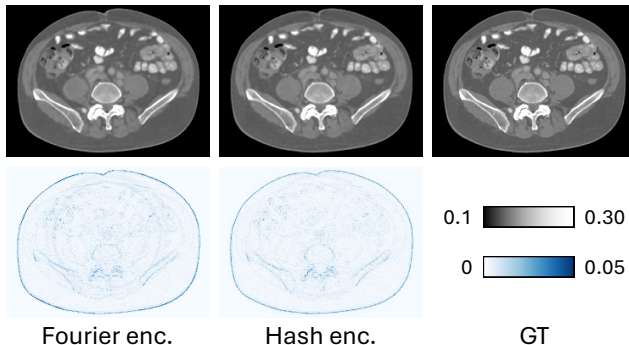


Figure 9. Qualitative results of our Riner ablating the MLP network on a test sample (#7) of DeepLesion dataset [57].

that the hash encoding [29] preserves more image details than the Fourier encoding [48].

In summary, the network architecture can impact the quality of the CT images. Employing advanced networks may further improve RAR reconstructions. However, we emphasize that even the conventional Fourier encoding [48] achieves satisfactory performance. This demonstrates that the improvements in our method are driven by our physical model characterizing the nonlinear IM and IR effects, rather than by the network architecture.

5. Conclusion and Limitation

In this paper, we propose Riner, a new approach for addressing the RAR problem in 3D X-ray CBCT. Unlike existing RAR techniques, we formulates a multi-parameter inverse problem to fundamentally address the physical causes of ring artifacts. Using a novel differential physical model, the proposed Riner simultaneously learns the neural field of the CT images and estimates the X-ray detector responses directly from raw measurements. Extensive experiments on five datasets demonstrate that our unsupervised method achieves SOTA RAR reconstructions.

Despite effectiveness, the efficiency of our method could be further improved. Riner requires case-specific optimizations as an unsupervised approach. In our experiments, reconstructing a 3D CT volume of $256 \times 256 \times 100$ takes approximately 15 minutes on an NVIDIA RTX 4070Ti GPU. Advanced encoding techniques, such as K -plane [15], or Gaussian splatting [19], may offer promising solutions for improving its efficiency.

References

- [1] Samuel G Armato III, Geoffrey McLennan, Luc Bidaut, Michael F McNitt-Gray, Charles R Meyer, Anthony P Reeves, Binsheng Zhao, Denise R Aberle, Claudia I Henschke, Eric A Hoffman, et al. The lung image database consortium (lidc) and image database resource initiative (idri): a completed reference database of lung nodules on ct scans. *Medical physics*, 38(2):915–931, 2011. [5](#), [6](#), [7](#), [1](#), [2](#), [3](#), [4](#)
- [2] Beer. Bestimmung der absorption des rothen lichts in farbigen flüssigkeiten. *Annalen der Physik*, 162(5):78–88, 1852. [3](#)
- [3] Lukas Birklein, Elmar Schömer, Robert Brylka, Ulrich Schwanecke, and Ralf Kurt Willy Schulze. Neural deformable cone beam ct. *Eurographics*, 2023. [3](#)
- [4] F Edward Boas, Dominik Fleischmann, et al. Ct artifacts: causes and reduction techniques. *Imaging Med*, 4(2):229–240, 2012. [1](#), [2](#), [3](#)
- [5] Yuanhao Cai, Jiahao Wang, Alan Yuille, Zongwei Zhou, and Angtian Wang. Structure-aware sparse-view x-ray 3d reconstruction. In *Proceedings of the IEEE/CVF Conference on Computer Vision and Pattern Recognition*, pages 11174–11183, 2024. [3](#)
- [6] Shaojie Chang, Xi Chen, Jiayu Duan, and Xuanqin Mou. A cnn-based hybrid ring artifact reduction algorithm for ct images. *IEEE Transactions on Radiation and Plasma Medical Sciences*, 5(2):253–260, 2020. [1](#), [2](#), [4](#), [5](#), [6](#), [7](#)
- [7] YM Chen and JQ Liu. An iterative numerical algorithm for solving multi-parameter inverse problems of evolutionary partial differential equations. *Journal of Computational Physics*, 53(3):429–442, 1984. [2](#)
- [8] Zhuo Chen, Xiaoqi Xi, Yu Han, Siyu Tan, Chunhui Wang, Yanmin Sun, Lei Li, and Bin Yan. Research status and prospect of ring artifact correction method for x-ray ct. In *International Conference on Optoelectronic Information and Functional Materials (OIFM 2024)*, pages 245–252. SPIE, 2024. [2](#)
- [9] Michel Cristofol, Jimmy Garnier, François Hamel, and Lionel Roques. Uniqueness from pointwise observations in a multi-parameter inverse problem. *Communications on Pure and Applied Analysis*, 11(1):173–188, 2011. [2](#)
- [10] Matteo Dalla Riva, Paolo Luzzini, and Paolo Musolino. Multi-parameter analysis of the obstacle scattering problem. *Inverse Problems*, 38(5):055004, 2022. [2](#)
- [11] Alexey Dosovitskiy, Lucas Beyer, Alexander Kolesnikov, Dirk Weissenborn, Xiaohua Zhai, Thomas Unterthiner, Mostafa Dehghani, Matthias Minderer, Georg Heigold, Sylvain Gelly, et al. An image is worth 16x16 words: Transformers for image recognition at scale. In *International Conference on Learning Representations*, 2020. [2](#), [6](#), [1](#)
- [12] Chenhe Du, Xiyue Lin, Qing Wu, Xuanyu Tian, Ying Su, Zhe Luo, Hongjiang Wei, S Kevin Zhou, Jingyi Yu, and Yuyao Zhang. Dper: Diffusion prior driven neural representation for limited angle and sparse view ct reconstruction. *arXiv preprint arXiv:2404.17890*, 2024. [3](#)
- [13] Wei Fang, Liang Li, and Zhiqiang Chen. Removing ring artifacts for photon-counting detectors using neural networks in different domains. *IEEE access*, 8:42447–42457, 2020. [1](#), [2](#)
- [14] Lee A Feldkamp, Lloyd C Davis, and James W Kress. Practical cone-beam algorithm. *Josa a*, 1(6):612–619, 1984. [1](#), [3](#), [5](#), [7](#)
- [15] Sara Fridovich-Keil, Giacomo Meanti, Frederik Rahbæk Warburg, Benjamin Recht, and Angjoo Kanazawa. K-planes: Explicit radiance fields in space, time, and appearance. In *Proceedings of the IEEE/CVF Conference on Computer Vision and Pattern Recognition*, pages 12479–12488, 2023. [8](#)
- [16] Marcus J Grote and Uri Nahum. Adaptive eigenspace for multi-parameter inverse scattering problems. *Computers & Mathematics with Applications*, 77(12):3264–3280, 2019. [2](#)
- [17] Jakob S Jørgensen, Evelina Ametova, Genoveva Burca, Gemma Fardell, Evangelos Papoutsellis, Edoardo Pasca, Kris Thielemans, Martin Turner, Ryan Warr, William RB Lionheart, et al. Core imaging library-part i: a versatile python framework for tomographic imaging. *Philosophical Transactions of the Royal Society A*, 379(2204):20200192, 2021. [5](#), [1](#)
- [18] Avinash C Kak and Malcolm Slaney. *Principles of computerized tomographic imaging*. SIAM, 2001. [5](#), [7](#), [1](#)
- [19] Bernhard Kerbl, Georgios Kopanas, Thomas Leimkuehler, and George Drettakis. 3d gaussian splatting for real-time radiance field rendering. *ACM Trans. Graph.*, 42(4), 2023. [8](#)
- [20] Diederik P Kingma. Adam: A method for stochastic optimization. *arXiv preprint arXiv:1412.6980*, 2014. [4](#)
- [21] VS Kostsov. General approach to the formulation and solution of the multi-parameter inverse problems of atmospheric remote sensing with measurements and constraints of different types. *International Journal of Remote Sensing*, 36(11):2963–2994, 2015. [2](#)
- [22] Yiannis Kyriakou, Daniel Prell, and Willi A Kalender. Ring artifact correction for high-resolution micro ct. *Physics in medicine & biology*, 54(17):N385, 2009. [1](#), [7](#)
- [23] Jean-Henri Lambert. *Photometria sive de mensura et gradibus luminis, colorum et umbrae*. Sumptibus viduae Eberhardi Klett, typis Christophori Petri Detleffsen, 1760. [3](#)
- [24] Jooho Lee, Junhyun Ahn, and Jongduk Baek. Neural attenuation fields for metal artifact reduction in dental ct. In *Medical Imaging 2024: Physics of Medical Imaging*, pages 173–179. SPIE, 2024. [3](#)
- [25] Yiqun Lin, Zhongjin Luo, Wei Zhao, and Xiaomeng Li. Learning deep intensity field for extremely sparse-view cbct reconstruction. In *International Conference on Medical Image Computing and Computer-Assisted Intervention*, pages 13–23. Springer, 2023. [4](#)
- [26] Xiaojie Lv, Xuezhi Ren, Peng He, Mi Zhou, Zourong Long, Xiaodong Guo, Chengyu Fan, Biao Wei, and Peng Feng. Image denoising and ring artifacts removal for spectral ct via deep neural network. *IEEE access*, 8:225594–225601, 2020. [2](#)
- [27] Cynthia H McCollough, Adam C Bartley, Rickey E Carter, Baiyu Chen, Tammy A Drees, Phillip Edwards, David R Holmes III, Alice E Huang, Farhana Khan, Shuai Leng, et al. Low-dose ct for the detection and classification of metastatic liver lesions: results of the 2016 low dose ct grand challenge. *Medical physics*, 44(10):e339–e352, 2017. [5](#), [6](#), [7](#), [1](#), [2](#), [3](#), [4](#)

- [28] Ben Mildenhall, Pratul P Srinivasan, Matthew Tancik, Jonathan T Barron, Ravi Ramamoorthi, and Ren Ng. Nerf: Representing scenes as neural radiance fields for view synthesis. *Communications of the ACM*, 65(1):99–106, 2021. [2](#), [3](#), [4](#)
- [29] Thomas Müller, Alex Evans, Christoph Schied, and Alexander Keller. Instant neural graphics primitives with a multiresolution hash encoding. *ACM transactions on graphics (TOG)*, 41(4):1–15, 2022. [4](#), [8](#)
- [30] Beat Münch, Pavel Trtik, Federica Marone, and Marco Stamparoni. Stripe and ring artifact removal with combined wavelet—fourier filtering. *Optics express*, 17(10):8567–8591, 2009. [2](#), [4](#), [5](#), [1](#)
- [31] Maxime Nauwynck, Shabab Bazrafkan, AH van Heteren, Jan De Beenhouwer, and Jan Sijbers. Ring artifact reduction in sinogram space using deep learning. In *The 6th International Conference on Image Formation in X-Ray Computed Tomography, 3-7 August, 2020, Regensburg, Germany*, pages 486–489, 2020. [2](#)
- [32] Evangelos Papoutsellis, Evelina Ametova, Claire Delplancke, Gemma Fardell, Jakob S Jørgensen, Edoardo Pasca, Martin Turner, Ryan Warr, William RB Lionheart, and Philip J Withers. Core imaging library-part ii: multichannel reconstruction for dynamic and spectral tomography. *Philosophical Transactions of the Royal Society A*, 379(2204):20200193, 2021. [5](#), [1](#)
- [33] Adam Paszke, Sam Gross, Francisco Massa, Adam Lerer, James Bradbury, Gregory Chanan, Trevor Killeen, Zeming Lin, Natalia Gimelshein, Luca Antiga, et al. Pytorch: An imperative style, high-performance deep learning library. *Advances in neural information processing systems*, 32, 2019. [4](#)
- [34] Daniel Prell, Yiannis Kyriakou, and Willi A Kalender. Comparison of ring artifact correction methods for flat-detector ct. *Physics in Medicine & Biology*, 54(12):3881, 2009. [1](#), [2](#), [3](#)
- [35] Nasim Rahaman, Aristide Baratin, Devansh Arpit, Felix Draxler, Min Lin, Fred Hamprecht, Yoshua Bengio, and Aaron Courville. On the spectral bias of neural networks. In *International conference on machine learning*, pages 5301–5310. PMLR, 2019. [2](#), [4](#)
- [36] Sabrina Rashid, Soo Yeol Lee, and Md Kamrul Hasan. An improved method for the removal of ring artifacts in high resolution ct imaging. *EURASIP Journal on Advances in Signal Processing*, 2012:1–18, 2012. [1](#), [7](#)
- [37] Carsten Raven. Numerical removal of ring artifacts in microtomography. *Review of scientific instruments*, 69(8):2978–2980, 1998. [1](#), [2](#), [7](#)
- [38] Albert W Reed, Hyojin Kim, Rushil Anirudh, K Aditya Mohan, Kyle Champley, Jingu Kang, and Suren Jayasuriya. Dynamic ct reconstruction from limited views with implicit neural representations and parametric motion fields. In *Proceedings of the IEEE/CVF International Conference on Computer Vision*, pages 2258–2268, 2021. [3](#)
- [39] Erik L Ritman. Current status of developments and applications of micro-ct. *Annual review of biomedical engineering*, 13(1):531–552, 2011. [7](#)
- [40] Mark Rivers. Tutorial introduction to x-ray computed microtomography data processing. *University of Chicago*, 1998. [2](#), [5](#), [1](#)
- [41] Olaf Ronneberger, Philipp Fischer, and Thomas Brox. U-net: Convolutional networks for biomedical image segmentation. In *Medical image computing and computer-assisted intervention—MICCAI 2015: 18th international conference, Munich, Germany, October 5-9, 2015, proceedings, part III 18*, pages 234–241. Springer, 2015. [2](#), [6](#), [1](#)
- [42] Darius Rückert, Yuanhao Wang, Rui Li, Ramzi Idoughi, and Wolfgang Heidrich. Neat: Neural adaptive tomography. *ACM Transactions on Graphics (TOG)*, 41(4):1–13, 2022. [3](#)
- [43] William C Scarfe and Allan G Farman. What is cone-beam ct and how does it work? *Dental Clinics of North America*, 52(4):707–730, 2008. [1](#)
- [44] Liyue Shen, John Pauly, and Lei Xing. Nerp: implicit neural representation learning with prior embedding for sparsely sampled image reconstruction. *IEEE Transactions on Neural Networks and Learning Systems*, 35(1):770–782, 2022. [3](#), [4](#)
- [45] Ligen Shi, Chang Liu, Xu Jiang, YunZe Liu, Ping Yang, Shifeng Guo, and Xing Zhao. Ring artifacts removal based on implicit neural representation of sinogram data. *arXiv preprint arXiv:2409.15731*, 2024. [5](#), [6](#), [1](#)
- [46] Vincent Sitzmann, Julien Martel, Alexander Bergman, David Lindell, and Gordon Wetzstein. Implicit neural representations with periodic activation functions. *Advances in neural information processing systems*, 33:7462–7473, 2020. [4](#)
- [47] Yu Sun, Jiaming Liu, Mingyang Xie, Brendt Wohlberg, and Ulugbek S Kamilov. Coil: Coordinate-based internal learning for tomographic imaging. *IEEE Transactions on Computational Imaging*, 7:1400–1412, 2021. [1](#)
- [48] Matthew Tancik, Pratul Srinivasan, Ben Mildenhall, Sara Fridovich-Keil, Nithin Raghavan, Utkarsh Singhal, Ravi Ramamoorthi, Jonathan Barron, and Ren Ng. Fourier features let networks learn high frequency functions in low dimensional domains. *Advances in neural information processing systems*, 33:7537–7547, 2020. [4](#), [8](#)
- [49] Sofya Titarenko, Philip J Withers, and Anatoly Yagola. An analytical formula for ring artefact suppression in x-ray tomography. *Applied Mathematics Letters*, 23(12):1489–1495, 2010. [2](#)
- [50] Philip Trapp, Carlo Amato, Stefan Sawall, Marc Kachelrieß, and Tim Vöth. Deepprar: a cnn-based approach for ct and cbct ring artifact reduction. In *Medical Imaging 2022: Physics of Medical Imaging*, pages 337–344. SPIE, 2022. [1](#), [2](#), [4](#), [5](#), [6](#)
- [51] Elluru Venkatesh and Snehal Venkatesh Elluru. Cone beam computed tomography: basics and applications in dentistry. *Journal of istanbul University faculty of Dentistry*, 51(3 Suppl 1):102–121, 2017. [1](#)
- [52] Nghia T Vo, Robert C Atwood, and Michael Drakopoulos. Superior techniques for eliminating ring artifacts in x-ray micro-tomography. *Optics express*, 26(22):28396–28412, 2018. [2](#), [4](#), [5](#), [6](#), [7](#), [1](#)
- [53] Qing Wu, Lixuan Chen, Ce Wang, Hongjiang Wei, S Kevin Zhou, Jingyi Yu, and Yuyao Zhang. Unsupervised polychromatic neural representation for ct metal artifact reduc-

- tion. *Advances in Neural Information Processing Systems*, 36:69605–69624, 2023. 3
- [54] Qing Wu, Ruimin Feng, Hongjiang Wei, Jingyi Yu, and Yuyao Zhang. Self-supervised coordinate projection network for sparse-view computed tomography. *IEEE Transactions on Computational Imaging*, 9:517–529, 2023. 3, 4
- [55] Qing Wu, Xu Guo, Lixuan Chen, Dongming He, Hongjiang Wei, Xudong Wang, S Kevin Zhou, Yifeng Zhang, Jingyi Yu, and Yuyao Zhang. Unsupervised density neural representation for ct metal artifact reduction. *arXiv preprint arXiv:2405.07047*, 2024. 3
- [56] Zhi-Qin John Xu, Yaoyu Zhang, and Tao Luo. Overview frequency principle/spectral bias in deep learning. *Communications on Applied Mathematics and Computation*, pages 1–38, 2024. 2
- [57] Ke Yan, Xiaosong Wang, Le Lu, Ling Zhang, Adam P Harrison, Mohammadhadi Bagheri, and Ronald M Summers. Deep lesion graphs in the wild: relationship learning and organization of significant radiology image findings in a diverse large-scale lesion database. In *Proceedings of the IEEE Conference on Computer Vision and Pattern Recognition*, pages 9261–9270, 2018. 4, 5, 6, 7, 8, 1, 2, 3
- [58] Xiaocheng Yang, Zhenyi Yang, Jingye Yan, Lin Wu, and Mingfeng Jiang. Multi-parameter regularization method for synthetic aperture imaging radiometers. *Remote Sensing*, 13(3):382, 2021. 2
- [59] MA Yousuf and M Asaduzzaman. An efficient ring artifact reduction method based on projection data for micro-ct images. *Journal of Scientific Research*, 2(1):37–45, 2010. 1, 7
- [60] Syed Waqas Zamir, Aditya Arora, Salman Khan, Munawar Hayat, Fahad Shahbaz Khan, and Ming-Hsuan Yang. Restormer: Efficient transformer for high-resolution image restoration. In *Proceedings of the IEEE/CVF conference on computer vision and pattern recognition*, pages 5728–5739, 2022. 1, 2, 4, 5, 6
- [61] Guangming Zang, Ramzi Idoughi, Rui Li, Peter Wonka, and Wolfgang Heidrich. Intratomo: self-supervised learning-based tomography via sinogram synthesis and prediction. In *Proceedings of the IEEE/CVF International Conference on Computer Vision*, pages 1960–1970, 2021. 3, 4
- [62] Ruyi Zha, Yanhao Zhang, and Hongdong Li. Naf: neural attenuation fields for sparse-view cbct reconstruction. In *International Conference on Medical Image Computing and Computer-Assisted Intervention*, pages 442–452. Springer, 2022. 3, 4
- [63] You Zhang, Hua-Chieh Shao, Tinsu Pan, and Tielige Mengke. Dynamic cone-beam ct reconstruction using spatial and temporal implicit neural representation learning (stirr). *Physics in Medicine & Biology*, 68(4):045005, 2023. 3
- [64] Liyan Zhu, Yue Cui, Yanxia Du, Dong Wei, and Youjun Deng. Research on the multi-parameter identification of thermal-acoustic-solid coupling problem in an inhomogeneous medium. *Journal of Mathematical Analysis and Applications*, 521(2):126920, 2023. 2

Unsupervised Multi-Parameter Inverse Solving for Reducing Ring Artifacts in 3D X-Ray CBCT

Supplementary Material

6. Additional Details of Datasets

In this work, we perform extensive experiments to evaluate our method on five datasets. For the three simulated datasets (DeepLesion [57], LIDC [1], and AAPM [27]), we follow the data simulation pipelines from previous RAR studies [6, 50, 52] to simulate non-ideal X-ray detectors for generating CT measurements. Specifically, three types of detectors are considered: ideal detectors with full signal responses, non-ideal detectors with fluctuating signal responses ($\alpha_s \in [0.75, 1.25]$), and defective detectors without signal responses (*i.e.*, $\alpha_s = 0$). We assume the number of photons emitted by the X-ray source is 1×10^7 . We implement equidistant 2D FBCT and equidistant 3D CBCT setups by using the Python library CIL [17, 32]. Moreover, noise is included in the CT measurement data. For the real-world data acquisition, we use a commercial Bruker SKYSCAN 1276 micro-CT scanner with standard CT protocols to scan our samples. Tab. 5 shows detailed parameters of CT acquisitions.

7. Additional Details of Baselines

In our experiments, we compare our method with eight well-known techniques representing the SOTA solution for the CT RAR problem. Here, we present the implementation details of these baselines for improved reproducibility.

FBP/FDK FBP [18]/FDK [14] are analytical linear reconstruction algorithms for 2D and 3D CT imaging. In our experiments, we implement them using the Python library CIL [17, 32] (<https://tomographicimaging.github.io/CIL/>).

Norm Norm, developed by Rivers [40], is a classical CT RAR algorithm. We use the Python library `Algotom` to implement it (<https://github.com/algotom/algotom>).

WaveFFT WaveFFT [30] is a well-known filter-based CT RAR algorithm, where raw CT measurements are processed with well-designed filters in the Fourier domain. In our experiment, we use the Python library `Algotom` to implement it (<https://github.com/algotom/algotom>).

Super Super, proposed by Vo, Nghia T., et al. [52], represents the SOTA in traditional non-deep learning (non-DL)

CT RAR models. This technique comprehensively models various types of ring artifacts and designs specific algorithms to address them. In our experiments, we use its official implementation (<https://github.com/algotom/algotom>).

HyUNet Chang et al.[6] pioneeringly proposed using convolutional neural networks (CNNs) to learn the unknown mapping from artifact-corrupted images to artifact-free outputs. By constructing a large-scale dataset consisting of extensive pairs of clear and ring-artifact-corrupted images, they trained a five-layer CNN, named HyUNet. In our experiment, we follow the original paper to implement and train the model using the training and validation sets from the DeepLesion dataset[57], from scratch with carefully tuned hyperparameters.

DeepRAR DeepRAR [50] is a supervised DL method designed for the CT RAR problem. It trains a residual UNet [41] to map artifact-corrupted CT images to ring artifacts. In our experiments, we reproduce and train it from scratch using the training and validation sets from the DeepLesion dataset [57], with carefully tuned hyperparameters.

Restormer Restormer [60] is a versatile supervised DL model designed for various low-level vision tasks, such as image denoising and super-resolution. It leverages an efficient ViT [11] architecture to restore high-resolution images using large-scale paired datasets. Benefiting from the ability of ViT [11] to capture both local and global image patterns, Restormer [60] achieves exceptional reconstruction performance. In our experiments, we utilize its official implementation (<https://github.com/swz30/Restormer>) and train it on the training and validation sets from the Deeplesion dataset [57] from scratch with carefully tuned hyperparameters.

SinoRAR SinoRAR [45] is an unsupervised method based on implicit neural representation for 2D CT RAR. Following CoIL [47], it uses two MLP networks to learn clean CT measurements and strip artifacts. By incorporating handcrafted priors, SinoRAR can recover clean CT measurements, thus enabling CT RAR reconstructions. In our experiments, we reproduce this method following the original paper.

Table 5. Detailed parameters of the acquisition geometry for five datasets used in our experiments.

Parameters	Simulated Datasets			Real-World Datasets	
	DeepLesion [57]	LIDC [1]	AAPM [27]	Walnut	Chicken foot
Manufacturer	N/A	N/A	N/A	BRUKER	BRUKER
Type of geometry	2D FBCT	2D FBCT	3D CBCT	2D FBCT	3D CBCT
Image Size	256×256	256×256	256×256×100	512×512	512×512×80
Voxel Size (mm ² /mm ³)	1×1	1×1	1×1×1	0.06×0.06	0.06×0.06×0.06
View Range (°)	[0, 360)	[0, 360)	[0, 360)	[0, 360)	[0, 360)
Source Voltage (kV)	N/A	N/A	N/A	100	60
Source Current (uA)	N/A	N/A	N/A	200	200
Exposure Time (ms)	N/A	N/A	N/A	276	250
Number of Detectors	500	500	300×200	720	120×1008
Detector Spacing (mm)	2	2	2	0.069	0.069
Number of Projection Views	360	360	360	720	720
Distance from Source to Center (mm)	370	370	300	92.602	92.602
Distance from Center to Detector (mm)	370	370	300	65.946	65.946

8. Additional Visualization Comparisons

Fig. 10 and Fig. 11 show more qualitative comparisons of our Riner and baselines.

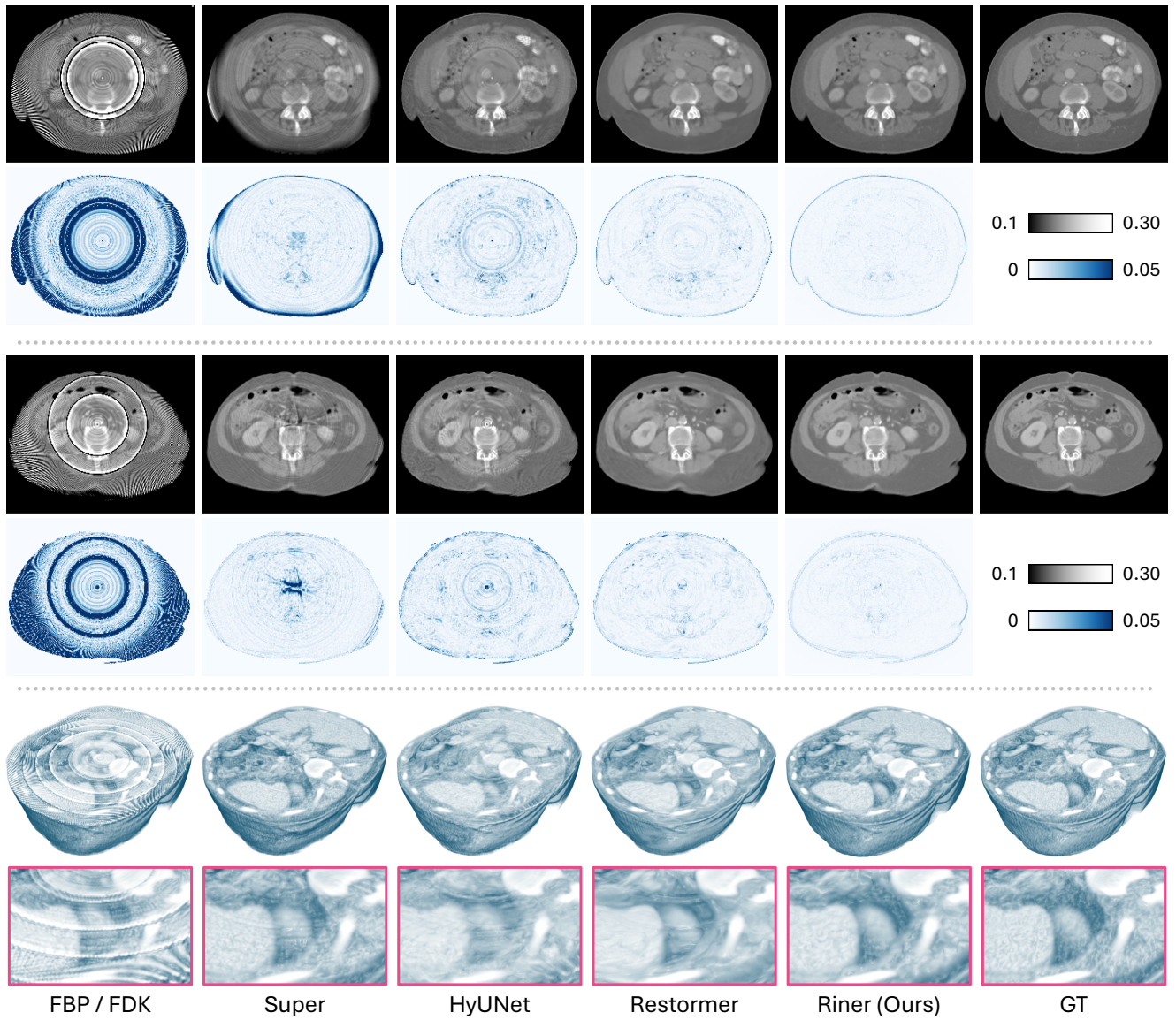


Figure 10. Qualitative results of our Riner and baselines on three representative samples of three simulated datasets (2D FBCT DeepLesion [57] and 2D FBCT LIDC [1], and 3D CBCT AAPM [27]).

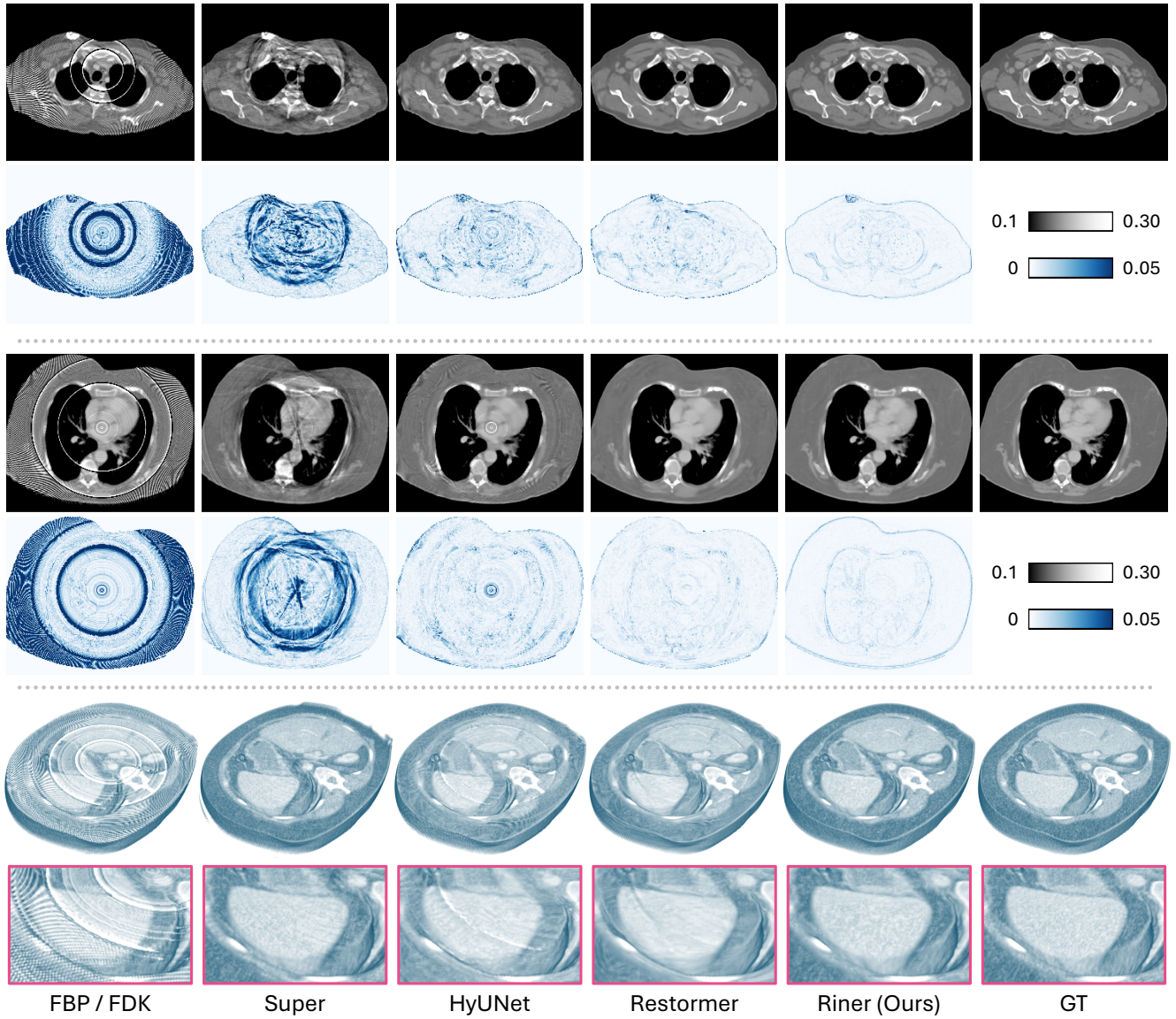


Figure 11. Qualitative results of our Riner and baselines on three representative samples of three simulated datasets (2D FBCT DeepLesion [57] and 2D FBCT LIDC [1], and 3D CBCT AAPM [27]).